Check for updates

Electrical, magnetic and magnetotransport properties of Na and Mo doped $Ca_3Co_4O_9$ materials

Uzma Hira,[ab] Jean-Claude Grivel,[b] Dennis Valbjørn Christensen,[b] Nini Pryds[b] and Falak Sher [ID] *[a]

We report the electrical, magnetic and magnetotransport properties of Na and Mo dual doped $Ca_{3-2x}Na_{2x}Co_{4-x}Mo_xO_9$ ($0 \leq x \leq 0.15$) polycrystalline samples. The results indicate that the strength of ferrimagnetic interaction decreases with increase in doping, as is evident from the observed decrease in Curie temperatures (T_C). The substitution of non-magnetic Mo^{6+} ions ($4d^0$) in CoO_2 layers and the presence of oxygen vacancies are responsible for decrease in ligand field strength, which results in an enhanced magnetization in the low doped $x = 0.025$ sample due to a change from the low spin to partial high spin electron configuration. The electrical resistivity of samples exhibits a semiconducting-like behavior in the low temperature range, a strongly correlated Fermi liquid-like behavior in the intermediate temperature range, and an incoherent metal-like behavior in the temperature range 210–300 K. All the samples show a large negative magnetoresistance (MR) at low temperature with a maximum MR value of −59% for the $x = 0.025$ sample at 2 K and 16 T applied field. The MR values follow the observed trend in magnetization at 5 K and sharply increase below the Curie temperatures of the samples, suggesting that the ferrimagnetic interactions are mainly responsible for the decrease in electrical resistivity under an applied magnetic field.

1. Introduction

Layered cobaltites have attracted considerable attention from the scientific community after the discovery of a large thermoelectric (TE) response in $NaCo_2O_4$, $Bi_2Sr_2Co_2O_x$ and $Ca_3Co_4O_9$ compounds.[1–3] In this family of cobalt oxides, misfit-layered $Ca_3Co_4O_9$ is especially interesting due to its structural and chemical stabilities at relatively higher temperatures,[4] unusual thermoelectric properties: coexistence of a large Seebeck coefficient and a low metallic-like electrical resistivity,[5] and ferrimagnetic or very weak ferromagnetic-like properties at low temperatures.[6] In conventional TE materials, a large Seebeck coefficient is associated with low carrier concentrations, typically in the range of $\sim10^{19}$ cm^{-3}.[7] However, the carrier concentration in the $Ca_3Co_4O_9$ system can reach up to $\sim10^{21}$ cm^{-3} and yet it exhibits a significantly large Seebeck coefficient, in the range $\sim$100–150 $\mu V\ K^{-1}$ at 300 K. The unusual thermoelectric properties of cobaltites may be attributed to the entropy of localized spins,[8] the electronic correlations,[9] spin and charge frustrations,[10] and large effective mass in the vicinity of Mott metal–insulator transition.[11] Nevertheless, the interplay between electron correlations and transport properties of cobaltites is a very complex issue and is still not well understood.

The crystal structure of $Ca_3Co_4O_9$ consists of two alternating structural subsystems stacking along the c-axis: rocksalt-type Ca_2CoO_3 layers (with regular stacking of CaO–CoO–CaO sheets) and CdI_2-type CoO_2 sheets.[3] The two subsystems have the same lattice parameters a, c and β but different b, suggesting a "misfit" between the two subsystems. The b-axis length of rocksalt-type Ca_2CoO_3 subsystem is referred to as b_1 whereas the b-axis length of CdI_2-type CoO_2 subsystem is labeled as b_2.[12] The CoO_2 sheet consists of two-dimensional triangular lattice of Co ions formed by a network of edge-sharing CoO_6 octahedra, and is believed to dominate the transport and magnetic properties of $Ca_3Co_4O_9$ system. As a consequence of misfit layered structure, this system shows highly anisotropic physical properties.[13] It has been reported previously that doping at Ca-site of $Ca_3Co_4O_9$ only increases/decreases the carrier concentration and has little effect on the band structure of the system.[14] On the other hand, doping at Co-site, especially in CoO_2 layer, causes large changes in the band structure, transport and magnetic properties.[15]

In addition to unusual thermoelectric properties, the misfit layered $Ca_3Co_4O_9$ also exhibits complex and interesting magnetic and magnetotransport properties.[4,16] The temperature dependent susceptibility measurements showed two magnetic transitions in $Ca_3Co_4O_9$ system: a ferrimagnetic transition at 19 K and a spin-state transition around 380 K.[17] The Muon spin rotation and relaxation (μSR) experiments revealed the existence of an incommensurate spin-density-wave (IC-SDW) state with onset temperature $T_{SDW} \approx$ 100 K and transition width $\Delta T = 70$ K. It was reported in literature

[a]Department of Chemistry and Chemical Engineering, SBA School of Science and Engineering, Lahore University of Management Sciences (LUMS), Lahore, Pakistan. E-mail: fsher@lums.edu.pk; Tel: +92 42 3560 8131

[b]Department of Energy Conversion and Storage, Technical University of Denmark, Risø DTU, Denmark

that the ferrimagnetism is caused by the interlayer coupling whereas the IC-SDW propagates in-plane.[18] The electrical resistivity of $Ca_3Co_4O_9$ showed a metal–insulator (MI) transition at $T_{MI} \approx 80$ K with a semiconducting-like behavior below T_{MI}.[3] Limelette *et al.* reported a large negative magnetoresistance of -70% at 9 T applied field in single-crystal $Ca_3Co_4O_9$.[19] The magnetotransport properties of this system were interpreted in terms of superexchange and double exchange mechanisms between Co^{3+} and Co^{4+} ions in CoO_2 layers. However, the underlying physics of strongly correlated electron properties in $Ca_3Co_4O_9$ and related cobaltites is still debatable and needs to be explored further.

The electrical transport and magnetic properties of materials are closely related to each other due to the coupling between the charge and spin degrees of freedom. There are few studies on the effect of doping on magnetic and magnetotransport properties of $Ca_3Co_4O_9$. For example, the substitution of Sr, Y and Bi for Ca was reported to suppress the ferrimagnetism in $Ca_3Co_4O_9$;[18] the substitution of Ti for Co lead to an enhanced spin fluctuation and spin-glass behavior;[14] the substitution of Ag for Ca altered the correlated electron properties of $Ca_3Co_4O_9$;[20] and the substitution of rare-earth ions (R^{3+}) resulted in an increase of thermopower (S) due to the enhanced electron correlation.[13] In another study, it was reported that magnetic behavior of $Ca_3Co_4O_9$ changes from a ferrimagnetic to a spin-glass state with Mo doping.[21] Although the electrical transport and magnetic properties of materials are closely related to each other due to the coupling between the charge and spin degrees of freedom, there are not many research investigations on the magnetotransport properties of doped $Ca_3Co_4O_9$ cobaltites. In this context, we have studied the low-temperature magnetization, electrical resistivity and magnetoresistance of Na and Mo dual doped $Ca_3Co_4O_9$-based ceramic materials.

2. Experimental section

Polycrystalline samples of $Ca_{3-2x}Na_{2x}Co_{4-x}Mo_xO_9$ ($0 \leq x \leq 0.15$) were prepared by conventional solid-state reaction method. The stoichiometric quantities of $CaCO_3$ ($\geq 99.5\%$; Sigma-Aldrich), Co_3O_4 ($\geq 99.5\%$; Sigma-Aldrich) and $Na_2MoO_4 \cdot 2H_2O$ ($\geq 99.5\%$; Sigma-Aldrich) were thoroughly mixed and pressed into pellets and initially sintered at 700 °C for 8 h. The sintered pellets were ground into powders, pressed into pellets again and sintered twice at 900 °C for 8 h, with intermediate grinding and pelletizing, in air at a heating rate of 10 °C min^{-1} and then cooled down slowly to the room temperature.

The powder X-ray diffraction data (XRD) of all samples were collected using a Bruker D8 Advance diffractometer (Bruker, Germany) with Cu K$_\alpha$ ($\lambda = 1.5406$ Å) radiation at room temperature. The data were collected over an angular range $5° \leq 2\theta \leq 65°$ with a step size of $0.02°$. The microstructure of samples was examined with a FEI Nova NanoSEM 450 scanning electron microscope (SEM). The chemical compositions of all the samples were inspected through energy dispersive X-ray spectrometer (EDS, AZtec Oxford) coupled through scanning electron microscope.

Magnetic properties were measured using a cryogen-free vibrating sample magnetometer (VSM). The zero-field cooling (ZFC) and field cooling (FC) magnetizations were measured in the temperature range of 5 to 320 K under an applied field 0.1 T. The

magnetic hysteresis loops of all samples were measured at 5 K in the magnetic field range of 0 to ± 5 T. The Hall effect measurement setup from the Cryogenics was used to collect the transport data of samples in magnetic fields of up to 16 T and at various temperatures ranging from 2 to 300 K. The samples were cooled down in absence of an applied magnetic field, and the warm-up was performed in steps where the magnetic field was varied from 0 to ± 16 T at stabilized temperatures while measuring the magnetoresistance and Hall effect. Samples were contacted electrically at the corners using silver paste, and the van der Pauw method was used to extract the resistivity. In all cases the Hall coefficient was found to be linear.

3. Results and discussion

The crystal structures of $Ca_{3-2x}Na_{2x}Co_{4-x}Mo_xO_9$ ($0 \leq x \leq 0.15$) samples were analyzed by collecting powder X-ray diffraction data at room temperature. The XRD patterns (Fig. 1(a)) show that all samples are phase pure. All diffraction peaks could be indexed to the standard JCPDS card (21-139) and match well with the previously reported monoclinic crystal symmetry for $Ca_3Co_4O_9$ system.[3,5] The diffraction data was Rietveld analyzed

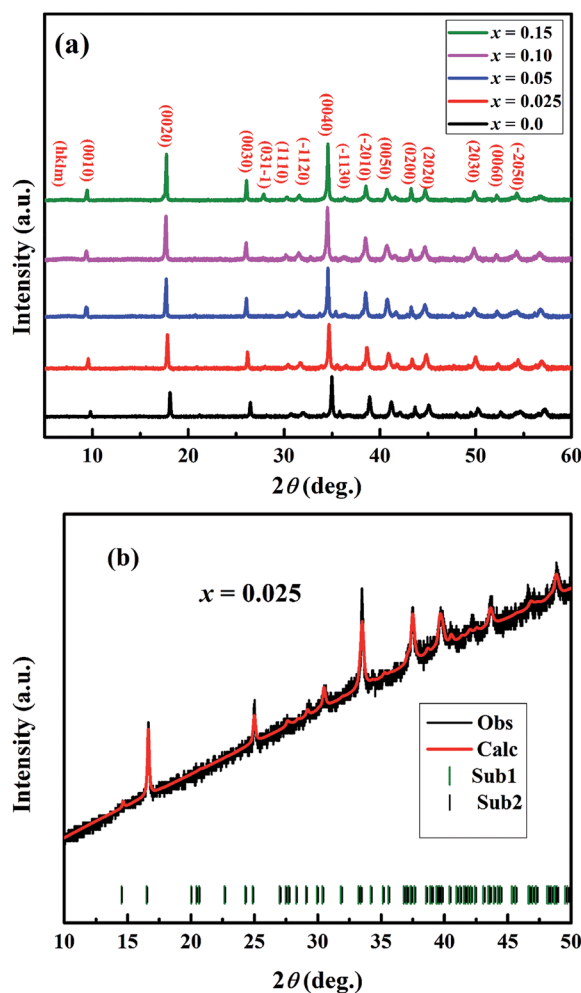**Fig. 1** (a) Powder XRD patterns of $Ca_{3-2x}Na_{2x}Co_{4-x}Mo_xO_9$ ($0 \leq x \leq 0.15$) samples. (b) Rietveld refined powder XRD pattern of $x = 0.025$ sample.

**Table 1** Crystallographic parameters for $Ca_{3-2x}Na_{2x}Co_{4-x}Mo_xO_9$ ($0 \leq x \leq 0.15$) samples obtained from the Rietveld refinement of powder X-ray diffraction data[a]

Composition $Ca_{3-2x}Na_{2x}Co_{4-x}Mo_xO9$	$x = 0.0$	$x = 0.025$	$x = 0.05$	$x = 0.10$	$x = 0.15$
Lattice parameters					
a (Å)	4.8229	4.8242	4.8254	4.8324	4.8380
b_1 (Å)	4.5453	4.5557	4.5607	4.5646	4.5698
b_2 (Å)	2.8215	2.8210	2.820	2.8131	2.8050
c (Å)	10.8327	10.8350	10.8369	10.8531	10.8621
β (deg.)	98.807	98.202	98.120	98.110	98.031
δ (b_1/b_2)	1.61	1.61	1.62	1.62	1.63
Volume, V_1 (Å)^3	234.7	235.7	236.1	236.7	237.8
Volume, V_2 (Å)^3	145.2	146.0	146.1	146.5	147.7
Reliability factors					
R_{wp} (%)	3.99	1.93	2.75	3.89	3.90
R_p (%)	3.25	1.46	2.23	3.18	3.21
GOF	3.29	1.66	2.49	2.62	2.43

[a] b_1 and b_2 are the b-axis lattice parameter for [Ca_2CoO_3] and [CoO_2] subsystems, respectively.

in the super space group $X2/m(0b0)s0$ using a computer program JANA 2006.[22] The refined XRD pattern for $Ca_{2.95}$-$Na_{0.05}Co_{3.975}Mo_{0.025}O_9$ sample is presented in Fig. 1(b) as an example, and the resulting structural parameters are summarized in Table 1. We have observed that diffraction peaks shift to lower angle values with increase in doping content (x). This result is consistent with the fact that ionic radii of the substituent Na^+ (1.02 Å) and Mo^{6+} (0.59 Å) ions are larger than ionic radii of the corresponding Ca^{2+} (1.00 Å) ions, and Co^{3+} (0.545 Å)/Co^{4+} (0.53 Å) ions in the six coordination number, respectively.[23] Fig. 2 shows the lattice parameters a, b_1, b_2, c and unit cell volume V_1 and V_2 as a function of doping content (x). The lattice parameters a, b_1, c and unit cell volumes V_1 and V_2 increase linearly with increase in the doping content of Na and Mo. However, the lattice parameter b_2 decreases with increase in dual doping. Overall, the refined cell parameters are in
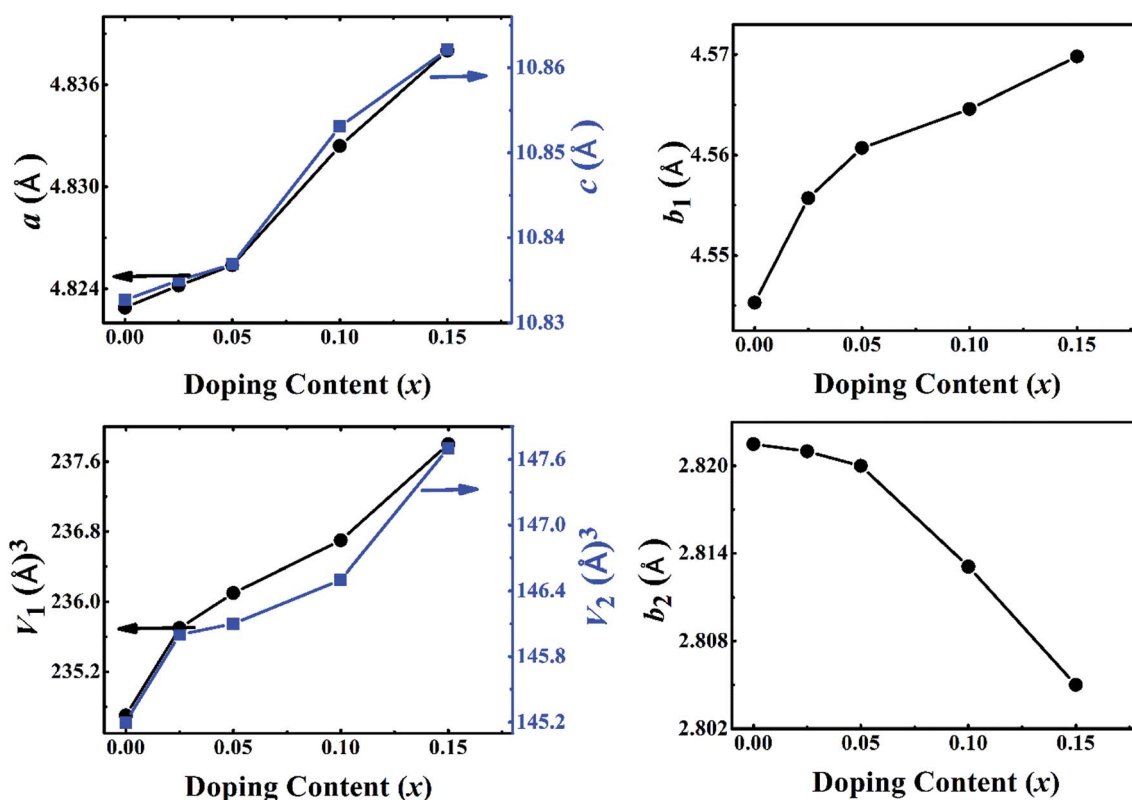
Fig. 2 Structural parameters a, b_1, b_2, c, V_1 and V_2 as a function of doping content (x) for $Ca_{3-2x}Na_{2x}Co_{4-x}Mo_xO_9$ ($0 \leq x \leq 0.15$) series.

agreement with the observed shifting of diffraction peaks to lower angle values as noted above. The values of quality factors like goodness of fit (GOF), weighted residual (R_{wp}) and residual of the least-squares refinement (R_p) (Table 1) are all within the acceptable statistical range, suggesting that the Rietveld refinement results are reliable.

The SEM micrographs (Fig. 3) indicate that particles are well connected with each other and have no specific shape. Similar surface morphology has been reported for samples prepared by the conventional solid-state reaction method in previous research work.[5] The average grain size increases from 0.83 μm ($x = 0.0$) to 4.50 μm ($x = 0.15$) with increase in doping content (x), which is in keeping with the low melting point of $Na_2MoO_4 \cdot 2H_2O$ precursor and the expected higher diffusion rate of reacting species at the sintering temperature resulting in larger grain sizes.

The temperature dependence of magnetization (M) in $Ca_{3-2x}Na_{2x}Co_{4-x}Mo_xO_9$ under zero-field-cooled (ZFC) and field-cooled (FC) modes (5–300 K) at an applied field of 0.1 T are shown in Fig. 4. It is evident from plot that all samples exhibit Curie–Weiss paramagnetic behavior in the high temperature range 30–300 K. Both the ZFC and FC curves for $x = 0.0$ sample start to rise up sharply as the temperature is decreased below ~19 K, suggesting a paramagnetic (PM) to ferrimagnetic (FIM)

transition. The sharp rise in magnetization curves for doped samples is observed at a lower temperature range 5–7 K. The PM–FIM transition temperatures (T_{FIM}) of samples were estimated from the points of inflection of dM/dT slopes (Fig. 4) and the obtained values are listed in Table 2. The T_{FIM} value for $x = 0.0$ sample is comparable to the reported data in literature.[17] The values of T_{FIM} decrease with increase in doping content (x). We can attribute this trend to the non-magnetic nature of Mo^{6+} (d^0) ions, and the structural distortions with increase in doping as both these factors are expected to weaken the ferromagnetic interactions. The ZFC and FC curves for the undoped sample separate from each other below 19 K which indicates the existence of magnetic inhomogeneity in the long range ferromagnetic ordering. Unlike some of the previous research studies,[21,24,25] our doped samples do not show any separation between the ZFC and FC curves in the measured temperature range 5–300 K. This observation suggests the absence of spin-glass (SG) or cluster-glass (CG) state in these samples. It is important to mention that these samples may show divergence between the ZFC and FC curves at temperatures well below the PM–FIM transition.

Fig. 5 shows the magnetic field dependent magnetization (M–H) curves (hysteresis loops) for all samples at 5 K. The maximum magnetization ($M_{5 K}$), coercivity (H_C) and remanent
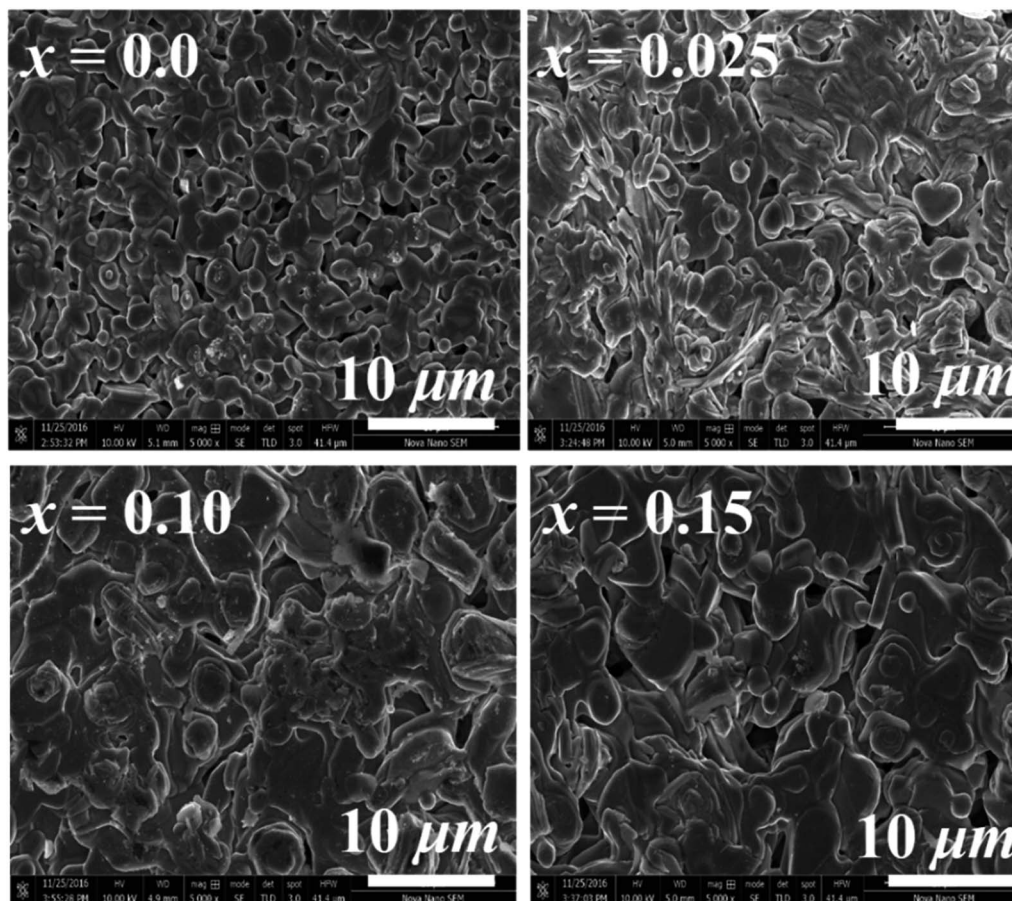

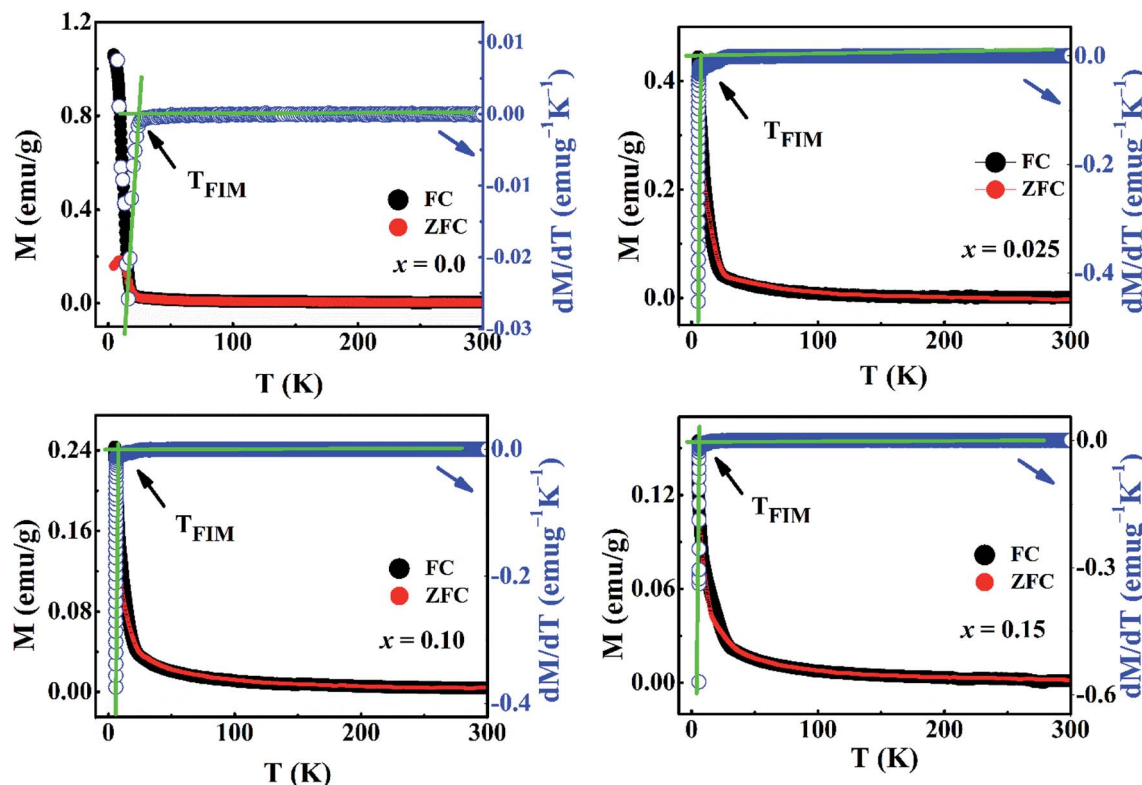**Fig. 3** SEM micrographs of $Ca_{3-2x}Na_{2x}Co_{4-x}Mo_xO_9$ ($0 \leq x \leq 0.15$) series.

Fig. 4 The temperature dependent zero-field-cooled (ZFC) and field-cooled (FC) magnetizations, along with slope dM/dT, for $Ca_{3-2x}Na_{2x}$-$Co_{4-x}Mo_xO_9$ ($0 \leq x \leq 0.15$) samples at 0.1 T applied magnetic field.

magnetization (M_r) of samples are listed in Table 2. It is evident that the magnetization does not saturate even at applied fields of up to 5 T, which suggests the presence of canted ferrimagnetism in our samples. The M–H curve of undoped sample exhibits a clear hysteresis loop, but it becomes smaller with increase in doping. The observed decrease in both coercivity and remanent magnetization suggests that our samples are becoming soft ferromagnet with Na and Mo dual doping. Similar results were reported in literature for In-doped $Ca_3Co_4O_9$ samples.[26] The values of $M_{5\,K}$ for all doped samples are higher than undoped $Ca_3Co_4O_9$ system, with a maximum value of 6.30 emu g^{-1} for $x = 0.025$ sample. As reported previously, ferrimagnetism in $Ca_3Co_4O_9$ is caused by the interlayer coupling between Ca_2CoO_3 and CoO_2 subsystems.[5,27] Both the superexchange and double exchange interactions between Co^{3+} and Co^{4+} ions were considered to coexist in CoO_2 layers. The substitution of Fe, Mn, In or Mo in $Ca_3Co_4O_9$ was found to

suppress the interlayer coupling and result in decrease of magnetization.[5,21,27] We believe that compositional inhomogeneities and presence of oxygen vacancies, which may be induced by the substitution of higher valent Mo^{6+} ions at Co-sites in $Ca_3Co_4O_9$ system, are responsible for the observed increase in $M_{5\,K}$ values in our doped samples, especially $x = 0.025$, as discussed in the next paragraph.

In order to analyze the magnetic data quantitatively, we fitted the inverse magnetic susceptibility with a Curie–Weiss law (Fig. 6), $\chi = C/(T - \theta_P)$, where χ is the molar magnetic susceptibility, C is the Curie constant, and θ_P is the Weiss temperature. The values of effective magnetic moment, μ_{eff} were calculated using the values of C obtained from the slopes of linear fits in Fig. 6. The obtained values of θ_P and μ_{eff} per Co ion are listed in Table 2. The negative values of θ_P suggest the presence of antiferromagnetic (or ferrimagnetic) interactions in these materials. The value of $\mu_{eff} = 1.30\ \mu_B$ for $x = 0.0$ sample is

Table 2 Important parameters obtained from the magnetization measurements of samples

Composition (x)	T_{FIM} (K)	C (emu K mol^{-1})	θ_P (K)	μ_B (μ_B)	M_S (kOe) at 5 K	M_r (emu g^{-1}) at 5 K	$M_{5\,K}$ (emu g^{-1})
0.0	19.0	0.2113	−55	1.30	190.0	2.25	4.64
0.025	6.7	0.6925	−42	2.35	24.21	0.63	6.30
0.10	6.3	0.5320	−48	2.06	21.99	0.47	4.96
0.15	5.3	0.3258	−60	1.61	17.04	0.20	4.85

Paper

RSC Advances
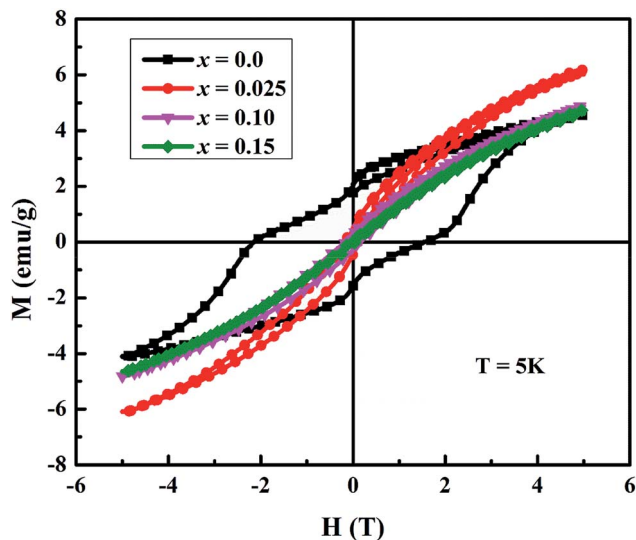
Fig. 5 The magnetization *vs.* applied magnetic field plots of Ca_{3-2x}-$Na_{2x}Co_{4-x}Mo_xO_9$ ($0 \leq x \leq 0.15$) samples at 5 K.

comparable to the literature data for $Ca_3Co_4O_9$ system.[17] However, the μ_{eff} values of 2.35, 2.06, and 1.61 μ_B per Co for $x = 0.025$, 0.10 and 0.15 samples respectively are higher than the undoped sample. We can discuss the observed magnetic moment data in terms of the average valence state of the Co in these materials. As we know, the electron configurations of Co^{2+}, Co^{3+} and Co^{4+} ions are $3d^7$, $3d^6$ and $3d^5$ respectively. In an octahedral crystal field splitting between t_{2g} and e_g states, Co ions can have either the high spin (HS) or low spin (LS) electron configuration. The HS electron configuration for Co^{2+}, Co^{3+} and Co^{4+} ions corresponds to $t_{2g}^5e_g^2$ ($S = 3/2$, $\mu_{eff} = 3.87$ μ_B), $t_{2g}^4e_g^2$ ($S = 2$, $\mu_{eff} = 4.90$ μ_B) and $t_{2g}^3e_g^2$ ($S = 5/2$, $\mu_{eff} = 5.92$ μ_B) respectively whereas the LS electron configuration for these ions gives $t_{2g}^6e_g^1$ ($S = 1/2$, $\mu_{eff} = 1.73$ μ_B), $t_{2g}^6e_g^0$ ($S = 0$, $\mu_{eff} = 0$ μ_B) and $t_{2g}^5e_g^0$ ($S = 1/2$, $\mu_{eff} = 1.73$ μ_B) respectively. In previous studies, it has been reported that the average valence state of Co ions in $Ca_3Co_4O_9$ system is between +3 and +4, and both Co^{3+} and Co^{4+} ions are predicted to be in LS state.[3,5,26] Using this information, the calculated values of μ_{eff} for our doped samples, especially $x = 0.025$, could be explained by considering an intermediate spin or partial high spin electron configuration for Co^{3+} and Co^{4+} ions. This is also consistent with the low temperature (5 K) magnetization values of doped samples under an applied field of 5 T as shown in Fig. 5. We can attribute this change, from LS to partial HS electron configuration, to oxygen vacancies and the substitution of Mo^{6+} ions in CoO_2 layers. The presence of oxygen vacancies would reduce the ligand field strength and therefore promote electrons to e_g states. As the number of oxygen vacancies does not change linearly with doping, the substitution of higher concentrations of non-magnetic Mo^{6+} ions ($4d^0$) would result in decrease of magnetic moment.

The electrical resistivity (ρ) of samples was measured as a function of temperature (2–300 K) under zero magnetic field and the obtained data are shown in Fig. 7(a). As reported

elsewhere,[5,28,29] the electrical resistivity of our samples can be divided into three distinct transport regimes in the measured temperature range. In the low temperature range, the electrical resistivity shows insulating behavior characterized by a negative slope ($d\rho/dT < 0$) up to a broad minimum around the metal–insulator transition temperature (T_{MI}), implying the existence of IC-SDW state.[18] As the temperature is further increased, the electrical resistivity exhibits metallic behavior ($d\rho/dT > 0$) with two different regimes. The first one is identified as a strongly correlated Fermi liquid regime, up to the temperature T^*, with the electrical resistivity varying as $\rho = \rho^0 + AT^2$ (Fig. 7(b)), and the second one is known as an incoherent metal (or "bad metal") regime.[27] In this description, T^* is the transition temperature from Fermi liquid to incoherent metal, ρ^0 is the residual resistivity owing to the domain boundaries and other temperature-independent scattering mechanisms,[30] A is called the Fermi liquid transport coefficient, and AT^2 refers to the electron–electron scattering mechanism of carriers. It has been observed that overall shapes of ρ–T curves remain almost the same, but the values of ρ, T_{MI} and T^* change with increase in doping (Table 3). It is found that ρ initially decreases with low doping ($x = 0.025$) and then increases with further increase in Na and Mo dual doping. We can explain this trend by variations in the particle size, carrier concentration (n), carrier mobility (μ), structural distortions, and oxygen vacancies with increase in doping. The longitudinal resistivity, ρ is a reciprocal of electrical conductivity, σ and is given by: $\rho^{-1} = \sigma = ne\mu$, where n, μ and e are the carrier concentration, carrier mobility and elementary charge, respectively. Compared to other samples, $x = 0.025$ has higher values of n and μ, and reasonably large average particle size, and therefore it has the lowest resistivity in this series. The values of n and μ decrease with further increase in doping content (x), and consequently the electrical resistivity increases for larger x values. The presence of oxygen vacancies and structural distortions play a detrimental role in the transport mechanism, and therefore may also be contributing factors in the observed increase of electrical resistivity for heavily doped samples.
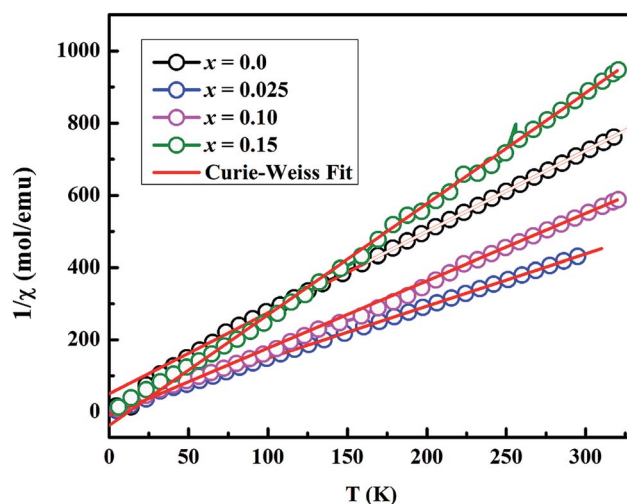

Fig. 6 The Curie–Weiss law fitting on magnetic data of $Ca_{3-2x}Na_{2x}$-$Co_{4-x}Mo_xO_9$ ($0 \leq x \leq 0.15$) samples.
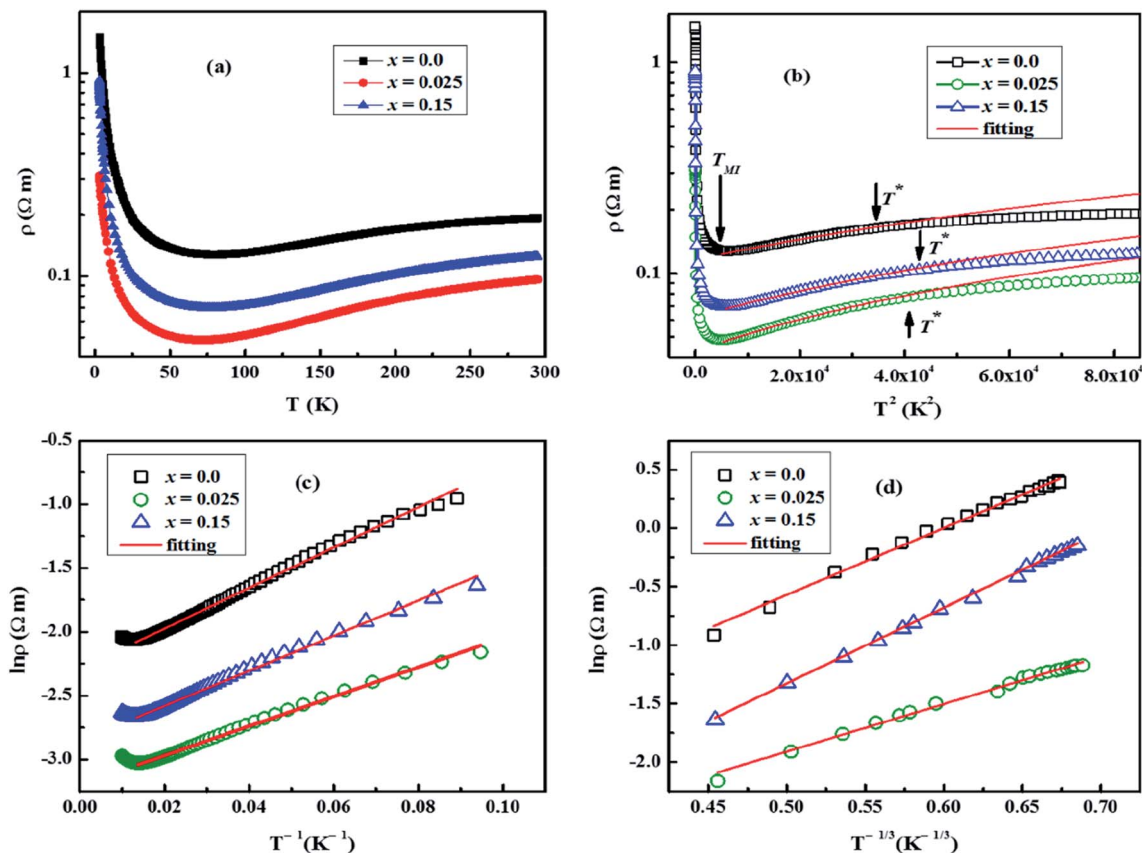
Fig. 7 (a) Temperature dependence of electrical resistivity (ρ). (b) Variation of ρ vs. T^2 for three samples. The solid lines are linear fitting using $\rho = \rho_A + AT^2$. The transition temperatures T_{MI} and T^* are marked by arrows. (c) Fitting plots of ρ–T curves according to the thermally activated model, and (d) fitting plots of ρ–T curves according to the 2D VRH model for $Ca_{3-2x}Na_{2x}Co_{4-x}Mo_xO_9$ ($0 \leq x \leq 0.15$) samples.

In order to investigate the effect of dual doping on electronic correlation in the Fermi liquid regime, we plotted $\rho(T)$ *versus* T^2 as shown in Fig. 7(b). The obtained fitting parameters of A (slope) and T^* (the end temperature on the ρ–T^2 linear fit) are listed in Table 3. The values of T_{MI} were taken as the temperature at which dρ/dT slope on ρ–T curves is equal to zero. It is found that the values of A and T_{MI} initially decrease for low doping ($x = 0.025$ sample) and then slightly increase with higher doping content (x). On the other hand, the values of T^* increase with increase in doping. The estimated values of A for all samples are comparable to the ones measured in heavy fermion compounds as reported elsewhere.[29] According to the dynamical mean field theory (DMFT) picture of the Fermi liquid,[5,31] a key role of effective mass m^* is predicted with $A \sim (m^*)^2$ and $T^* \sim 1/m^*$. Compared to the undoped sample, the observed decrease in values of A and increase of T^* both predict a decrease of m^* with doping. These results imply that the bandwidth of these compounds is increasing, and the electronic correlation is weakening with increase in doping.[5]

In order to investigate the effect of dual doping on strongly correlated electronic properties of these materials, we now look at the possible transport mechanisms. The temperature dependent electrical resistivity of cobaltites follows the thermally activated transport mechanism in the low-temperature insulating regime, as reported in literature.[32,33] It is given by

$$\rho(T) = \rho_0 \exp\left(\frac{\Delta E}{k_B T}\right) \quad (1)$$

where ρ_0 is a constant factor and ΔE is the activation energy. We tried to fit the low-temperature $\rho(T)$ data using eqn (1), and the results are shown in Fig. 7(c). We have found that ρ–T data can

Table 3 Hall effect, electrical resistivity and magnetoresistance parameters for $Ca_{3-2x}Na_{2x}Co_{4-x}Mo_xO_9$ ($0 \leq x \leq 0.15$) samples

Composition (x)	0.0	0.025	0.10	0.15
ρ (300 K) (10^{-5} Ω m)	22.5	10.5	14.0	16.0
n (300 K) (10^{19} cm^{-3})	5.09	6.39	5.23	3.71
μ (300 K) (cm^2 V^{-1} s^{-1})	0.64	1.02	0.963	0.78
T_{MI} (K)	88	73	—	76
T^* (K)	186	202	—	206
A (Ω m K^{-2})	1.44×10^{-6}	8.97×10^{-7}	—	1.03×10^{-6}
ΔE (meV)	1.36	1.18	—	0.99
T_0 (K)	67.1	269.6	—	186.2
m^*/m_o	9.83	8.94	—	8.74
MR (%) at 2 K & 16 T	−34	−59	—	−49
MR (%) at 2 K & 7 T	−30	−55	—	−46
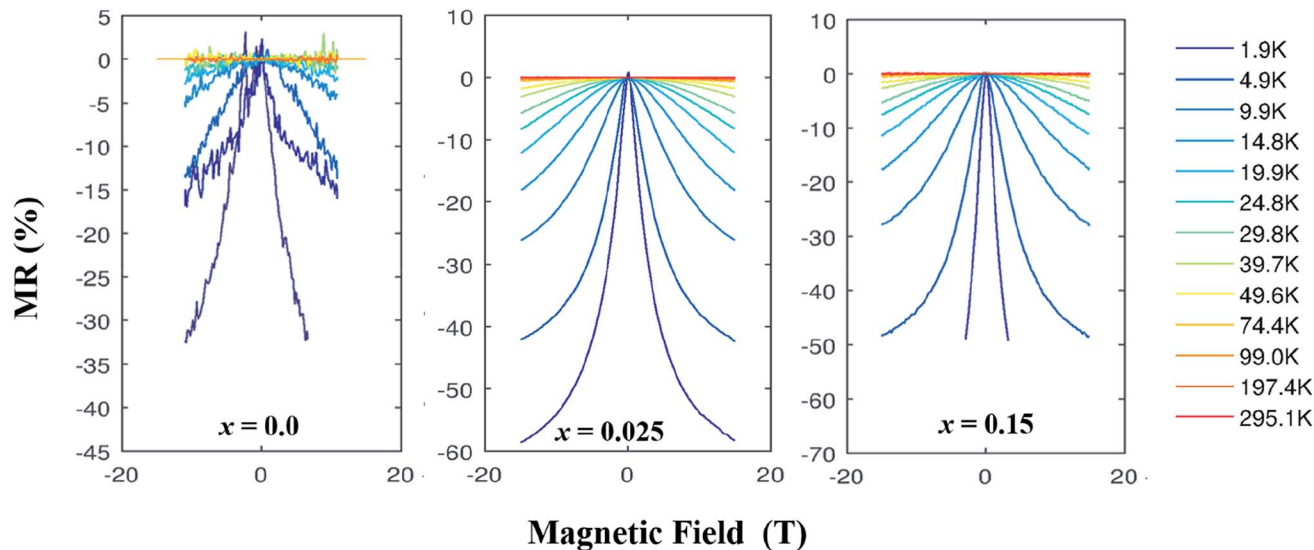
Fig. 8 MR (%) *vs.* applied field plots for $Ca_{3-2x}Na_{2x}Co_{4-x}Mo_xO_9$ ($0 \leq x \leq 0.15$) samples at different temperatures.

be fitted well for all samples by the thermally activated conduction model in the temperature range ~15–60 K. The obtained values of ΔE are listed in Table 3. The activation energy decreases with increase in doping content (x), suggesting that Na and Mo dual doping has a negative effect on the formation of SDW state. The variation of ΔE with doping indicates that the substitution of Mo is taking place mainly in CoO_2 layers of $Ca_3Co_4O_9$ structure because if the substitution of Mo had occurred in Ca_2CoO_3 layers then it would have no or little effect on the activation energy of materials.[34]

As mentioned above, the thermally activated conduction mechanism does not model the $\rho(T)$ data of our samples well below ~15 K. The Mott's two-dimensional variable range hopping model (2D VRH) gives the best fitting to the low-temperature $\rho(T)$ data. According to the 2D VRH model, the relation between electrical resistivity and temperature can be expressed as

$$\rho(T) = \rho(0) \exp\left(\frac{T_0}{T}\right)^{1/3} \qquad (2)$$

where $\rho(0)$ is a constant, $T_0 = 8/[\pi k_B N(\varepsilon_F) l_v^2]$ is the VRH characteristic temperature associated with the density of localized states at the Fermi energy $N(\varepsilon_F)$, l_v is the localization length and k_B is the Boltzmann constant.[35] The linear relationship of ln $\rho(T)$ *versus* $T^{-1/3}$ (Fig. 7(d)) shows that 2D VRH model fits well to the low-temperature, below 15 K, $\rho(T)$ data. The values of fitted parameter T_0 for samples are listed in Table 3. We can see that the values of T_0 are larger for doped samples than the undoped $Ca_3Co_4O_9$ system, which implies that the values of localization length l_v are smaller for doped samples. The reduction of localization length indicates stronger carrier localization or decreased carrier mobility in these materials. Similar results have been reported in previous studies on doped $Ca_3Co_4O_9$ system as well.[5,27] The VRH mechanism is two-dimensional, rather than the usual three-dimensional as found in many isotropic semiconductors, due to the anisotropic layered

structure of these cobaltites. Moreover, the carriers gain sufficient energy as the temperature is increased, and the transport mechanism gradually changes from 2D VRH to thermally activated conduction.[36]

We have measured the electrical resistivity of three samples ($x = 0.0$, 0.025 and 0.5) using a standard four-probe method as a function of applied magnetic field. Fig. 8 shows the field-dependent MR[$= \{\rho(H) - \rho(0)\}/\rho(0)$] data of samples at various temperatures in magnetic fields up to 16 T. A large negative MR is observed in all samples (Table 3), which is comparable to the reported values in single crystal $Ca_3Co_4O_9$ system. The $x = 0.025$ sample shows especially very large negative MR value of −59% at ~2 K and 16 T applied field. This is consistent with the observed larger magnetization of this sample. The large negative MR is a result of reduced spin scattering in the ferromagnetic state, which reflects a spin polarized electronic transport. The reduction of spin scattering originates from the strong electron correlation, which can be anticipated to increase below the ferrimagnetic transition. Our samples show noticeable magnetoresistances at all temperatures below ~50 K and the values of MR increase with decrease in temperature, with a maximum MR value at 2 K. This is unlike the colossal magnetoresistances observed in manganites[35] and $LnBaCo_2O_{5+\delta}$,[37] where a maximum of MR occurs near their Curie temperature or the metal-to-insulator transition temperature. This indicates that ferromagnetic interactions are weak in these materials. The negative MR increases abruptly below the relevant Curie temperature of samples. These results suggest that the ferrimagnetic correlation in the conducting layers is mainly responsible for the observed large negative MR in these materials.

4. Conclusions

We have investigated the effect of Na and Mo dual doping on magnetization, electrical resistivity and magnetoresistance of

$Ca_{3-2x}Na_{2x}Co_{4-x}Mo_xO_9$ ($0 \leq x \leq 0.15$) samples. The ZFC and FC curves reveal that the paramagnetic to ferrimagnetic transition temperature decreases with increase in doping content (x), indicating weakening of ferromagnetic interactions with increasing x. The observed increase in magnetization at low doping level can be attributed to change from low spin to partial high spin electron configuration with the substitution of non-magnetic Mo^{6+} ions ($4d^0$) in CoO_2 layers. The electrical resistivity of samples exhibits insulating behavior at low temperature, strongly correlated Fermi liquid type metallic behavior in the intermediate temperature range, and incoherent metal type behavior in the high temperature range. The strongly correlated electronic properties of these materials can be modeled by the Mott's two-dimensional variable range hopping model below ~15 K, thermally activated transport mechanism in the temperature range 15–60 K, and the relation $\rho = \rho^0 + AT^2$ in the Fermi liquid regime. The values of electrical resistivity follow the observed trend in carrier concentration, carrier mobility and particle size of doped samples. Large negative MR has been observed in all samples with a maximum value of -59% for $x = 0.025$ sample at 2 K and 16 T applied field. The sharp increase in MR below Curie temperature indicates that the ferrimagnetic interaction in the conducting layers is mainly responsible for the observed large negative magnetoresistances in these materials.

Conflicts of interest

There is no conflict of interest to declare.

Acknowledgements

References

1 I. Terasaki, Y. Sasago and K. Uchinokura, *Phys. Rev. B: Condens. Matter Mater. Phys.*, 1997, **56**, R12685.

2 F. Funahashi, I. Matsubara and S. Sodeoka, *Appl. Phys. Lett.*, 2000, **76**, 2385.

3 A. C. Masset, C. Michel, A. Maignan, M. Hervieu, O. Toulemonde, F. Studer, B. Reveau and J. Hejtmanek, *Phys. Rev. B: Condens. Matter Mater. Phys.*, 2000, **62**, 166.

4 H. Ohta, K. Sugiura and K. Koumoto, *Inorg. Chem.*, 2008, **47**, 8429.

5 Y. Wang, Y. Sui, P. Ren, L. Wang, X. Wang, W. Su and H. Fan, *Chem. Mater.*, 2010, **22**, 1155.

6 A. Pautrat, H. W. Eng and W. Prellier, *Phys. Rev. B: Condens. Matter Mater. Phys.*, 2005, **72**, 233405.

7 G. D. Mahan, *Solid State Phys.*, 1979, **51**, 81.

8 W. Koshibae, K. Tsutsui and S. Maekawa, *Phys. Rev. B: Condens. Matter Mater. Phys.*, 2000, **62**, 6869.

9 P. Limelette, S. Hébert, V. Hardy, R. Frésard, C. Simon and A. Maignan, *Phys. Rev. Lett.*, 2006, **97**, 046601.

10 O. I. Motrunich and P. A. Lee, *Phys. Rev. B: Condens. Matter Mater. Phys.*, 2004, **69**, 214516.

11 G. Pálsson and G. Kotliar, *Phys. Rev. Lett.*, 1998, **80**, 4775.

12 U. Hira, L. Han, K. Norrman, D. V. Christensen, N. Pryds and F. Sher, *RSC Adv.*, 2018, **8**, 12211.

13 J. Sugiyama, C. Xia and T. Tani, *Phys. Rev. B: Condens. Matter Mater. Phys.*, 2003, **67**, 104410.

14 Y. Wang, L. Xu, Y. Sui, X. Wang, J. Cheng and W. Su, *Appl. Phys. Lett.*, 2010, **97**, 062114.

15 B. C. Zhao, Y. P. Sun, W. J. Lu, X. B. Zhu and W. H. Song, *Phys. Rev. B: Condens. Matter Mater. Phys.*, 2006, **74**, 144417.

16 T. Yamamoto, K. Uchinokura and I. Tsukada, *Phys. Rev. B: Condens. Matter Mater. Phys.*, 2002, **65**, 184434.

17 J. Sugiyama, J. H. Brewer, E. J. Ansaldo, H. Itahara, K. Dohmae, Y. Seno, C. Xia and T. Tani, *Phys. Rev. B: Condens. Matter Mater. Phys.*, 2003, **68**, 134423.

18 J. Sugiyama, H. Itahara, T. Tani, J. H. Brewer and E. J. Ansaldo, *Phys. Rev. B: Condens. Matter Mater. Phys.*, 2002, **66**, 134413.

19 P. Limelette, J. C. Soret, H. Muguerra and D. Grebille, *Phys. Rev. B: Condens. Matter Mater. Phys.*, 2008, **77**, 245123.

20 Y. Wang, Y. Sui, J. G. Cheng, X. J. Wang and W. H. Su, *J. Phys.: Condens. Matter*, 2007, **19**, 356216.

21 Y. Fu, B. Zhao, Y. Huang, J. Yang, J. Dai, M. Zhou and Y. Sun, *Solid State Commun.*, 2011, **151**, 933.

22 M. D. Petricek and L. Palatinous, *JANA2006, The Crstallographic Computing System*, Institute of Physics, Praha, Czech Republic, 2006.

23 R. D. Shannon, *Acta Crystallogr., Sect. A: Cryst. Phys., Diffr., Theor. Gen. Crystallogr.*, 1976, **32**, 751.

24 B. C. Zhao, Y. P. Sun and W. H. Song, *J. Appl. Phys.*, 2006, **99**, 073906.

25 Y. Huang, B. Zhao, R. Ang, S. Lin, W. Song and Y. Sun, *J. Alloys Compd.*, 2013, **574**, 233.

26 Y. Huang, B. Zhao, R. Ang, S. Lin, Z. Huang, L. Yin, S. Tan, Y. Liu, W. Song and Y. Sun, *J. Am. Ceram. Soc.*, 2013, **96**, 791.

27 Y. Wang, Y. Sui, J. Cheng, X. Wang, W. Su, X. Liu and H. J. Fan, *J. Phys. Chem. C*, 2010, **114**, 5174.

28 M. Shikano and R. Funahashi, *Appl. Phys. Lett.*, 2003, **82**, 1851.

29 P. Limelette, V. Hardy, P. Auban-Senzier, D. Jérome, D. Flahaut, S. Hebert, R. Frésard, C. Simon, J. Noudem and A. Maignan, *Phys. Rev. B: Condens. Matter Mater. Phys.*, 2005, **71**, 233108.

30 P. Schiffer, A. P. Ramirez, W. Bao and S.-W. Cheong, *Phys. Rev. Lett.*, 1995, **75**, 3336.

31 A. Georges, G. Kotliar, W. Krauth and M. J. Rozenberg, *Rev. Mod. Phys.*, 1996, **68**, 13.

32 U. Hira, N. Pryds and F. Sher, *J. Electron. Mater.*, 2019, **48**, 4618.

33 T. Fujii and I. Terasaki, *Chemistry, Physics, and Materials Science of Thermoelectric Materials: Beyond Bismuth Telluride*, Kluwer Academic/Plenum Publishers, New York, 2003.

34 G. Yang, Q. Ramasse and R. F. Klie, *Phys. Rev. B: Condens. Matter Mater. Phys.*, 2008, **78**, 153109.

35 J. L. Lan, Y. H. Lin, G. J. Li, S. L. Xu, Y. Liu, C. W. Nan and S. Zhao, *Appl. Phys. Lett.*, 2010, **96**, 192104.

36 B. Raveau, A. Maignan, C. Martin and M. Hervieu, *Chem. Mater.*, 1998, **10**, 2641.

37 C. Martin, A. Maignan, D. Pelloquin, N. Nguyen and B. Raveau, *Appl. Phys. Lett.*, 1997, **71**, 1421.